

Fingerprint-Enhanced Capacitive-Piezoelectric Flexible Sensing Skin to Discriminate Static and Dynamic Tactile Stimuli

William Navaraj and Ravinder Dahiya*

Inspired by the structure and functions of the human skin, a highly sensitive capacitive-piezoelectric flexible sensing skin with fingerprint-like patterns to detect and discriminate between spatiotemporal tactile stimuli including static and dynamic pressures and textures is presented. The capacitive-piezoelectric tandem sensing structure is embedded in the phalange of a 3D-printed robotic hand, and a tempotron classifier system is used for tactile exploration. The dynamic tactile sensor, interfaced with an extended gate configuration to a common source metal oxide semiconductor field effect transistor (MOSFET), exhibits a sensitivity of 2.28 kPa^{-1} . The capacitive sensing structure has non-linear characteristics with sensitivity varying from 0.25 kPa^{-1} in the low-pressure range ($< 100 \text{ Pa}$) to 0.002 kPa^{-1} in high pressure ($\approx 2.5 \text{ kPa}$). The output from the presented sensor under a closed-loop tactile scan, carried out with an industrial robotic arm, is used as latency-coded spike trains in a spiking neural network (SNN) tempotron classifier system. With the capability of performing a real-time binary naturalistic texture classification with a maximum accuracy of 99.45%, the presented bioinspired skin finds applications in robotics, prosthesis, wearable sensors, and medical devices.


to simultaneously perceive and differentiate between multiple tactile stimuli such as pressure, temperature, vibration, pain, etc.^[1b,2a,2e,3] Some of the present eSkins have used machine learning tools also to decipher the information from the data acquired by tactile sensors.^[4] In fact, machine learning to handle tactile data and neuromimicking hardware architectures has been gaining lot of interest recently^[4b,5] along with local data storage.^[6] While multifunctional sensing is an attractive attribute of eSkin, suitable pressure or force sensing is the most important for critical static/dynamic force feedback in robotics to execute various manipulation tasks.^[7] The simultaneous use of static and dynamic force feedback from the skin is central to humans during daily tasks.^[8] This is also reflected by the presence of a population of slow-adapting (SA) receptors (e.g., Merkel and Ruffini corpuscles) and fast-adapting (FA) receptors (e.g., Meissner and Pacinian corpuscles) in

1. Introduction

Sensory feedback, particularly from touching or physical contact, is critical for various interactive tasks involving robots and humans and tactile skin or eSkin is a crucial technology needed for this purpose.^[1] Various types of physical and chemical sensors have been developed recently and significant progress has been made in terms of their integration on large areas and flexible or conformable surfaces.^[2] With these features, eSkins have offered artificial systems (e.g., robotic/prosthetic hand) the ability

human skin (Figure 1), which respond to sustained and dynamic touch stimuli, respectively.^[9] Table S1, Supporting Information, summarizes the various receptors in the glabrous area of the human skin and their functionalities. Merkel cells (SA-I) and Meissner corpuscles (FA-I) are present closer to the surface of the glabrous skin with a high density of innervation and smaller receptive fields ($< 3 \text{ mm}$), whereas, Ruffini (SA-II) and Pacinian corpuscles (FA-II) are deeper in the skin with a lower innervation density and larger receptive fields. The distribution, functionalities, and other aspects have been reviewed in the past.^[9,10] SA-I (Merkel cells) are useful for sensing fine details, textures, and for the discrimination of tactile patterns (e.g., Braille and static patterns of up to $200 \mu\text{m}$ spatial resolution).^[11] FA-II (Pacinian) also aid in discriminating object textures during sliding motion of the fingers against the object's surface. SA-II are found to respond to tangential shear strain and any stretching effect that the skin experiences.^[10a] The spatiotemporal detection of tactile stimuli is critical in the object/texture discrimination or the slip between the skin and objects.^[12] The fingerprint patterns on the skin and the interlocked microstructures at the interface of epidermal and dermal layers also improve the perception of fine texture by amplifying the vibrotactile signals when the finger is scanned over a surface.^[13] However, most of the reported pressure sensors provide the perception of either static or dynamic

Dr. W. Navaraj, Prof. R. Dahiya
Bendable Electronics and Sensing Technologies Group
School of Engineering
University of Glasgow
G12 8QQ Glasgow, UK
E-mail: Ravinder.Dahiya@glasgow.ac.uk

 The ORCID identification number(s) for the author(s) of this article can be found under <https://doi.org/10.1002/aisy.201900051>.

© 2019 The Authors. Published by WILEY-VCH Verlag GmbH & Co. KGaA, Weinheim. This is an open access article under the terms of the Creative Commons Attribution License, which permits use, distribution and reproduction in any medium, provided the original work is properly cited.

DOI: 10.1002/aisy.201900051

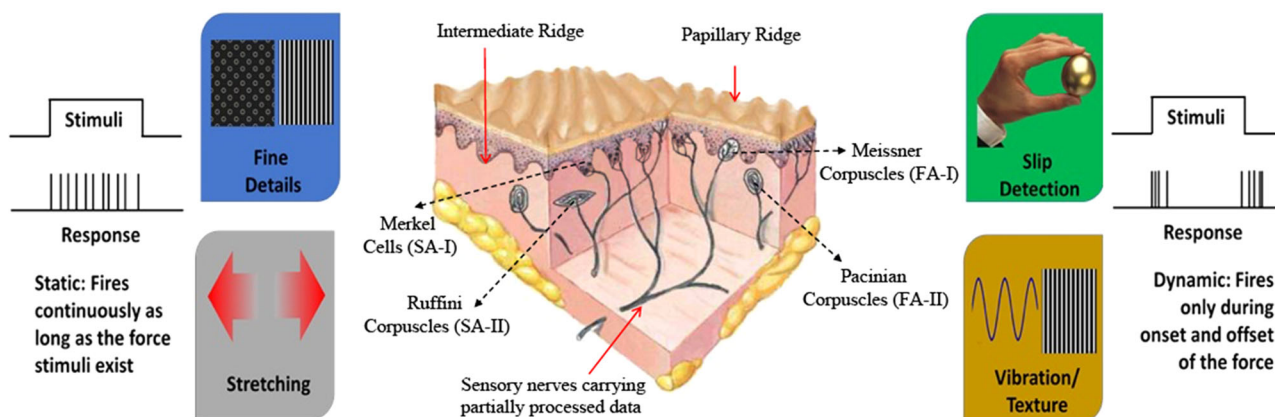


Figure 1. The MRs in the glabrous human skin which enable the tactile sensation. SA MRs (shown on the left) respond with continuous spikes during the static stimuli and the FA MRs (shown on the right) respond with spikes during the transition or the dynamic part of the stimuli.

pressure.^[14] A wide variety of advanced materials such as carbon nano-tubes (CNTs), organic polymers, graphene, and silicon have been explored for these sensors.^[2d,15] With robots expected to perform dexterous operations in an unstructured environment, or to autonomously perform the surgery, etc., it is critical to equip them with multifunctional sensors that also capture the static as well as dynamic contact events.

Here, by mimicking the structures and functions of the skin in human fingertips, we present a highly sensitive capacitive-piezoelectric flexible sensing skin with fingerprint-like patterns to detect and discriminate between spatiotemporal tactile stimuli including static and dynamic pressures and textures. The intrinsic inability of the piezoelectric sensors to detect sustained static pressures is overcome using the integrated capacitive sensor. Thus, the presented capacitive-piezoelectric sensor stack mimics the behavior of SA and FA mechanoreceptors (MRs) in human skin. The capacitive-piezoelectric tandem stack with fingerprint-like structures has been integrated on the phalange of a 3D-printed prosthetic hand. The fingerprint patterns used in the stack aid the detection of dynamic tactile patterns during surface scanning. Further, as proof of concept, we also show the neural-like processing tactile data from the sensing stack to mimic a real-world scenario where textures are distinguished by touching planar and nonplanar surfaces. **Figure 2a** shows the developed fingerprint-enhanced biomimicking tactile pattern recognition system. Similar to auditory perception, the texture perception in humans involves the spectral analysis of vibratory signals.^[16] Following this, we have used a biologically plausible wavelet transform^[17] to encode the sensor stack output into spike trains based on the leaky integrate-and-fire (LIF) model. Spike trains were classified using a tempotron classifier, using a biologically observed spike time-dependent plasticity (STDP) mechanism-based learning rule. Unlike prior work, which involved textures on the planar surface only, our approach allowed us to scan textures on nonplanar curved surfaces too. This is achieved by the proportional closed-loop control of the index finger of a 3D-printed hand attached to a 6-degrees-of-freedom (dof) UR5 robot to maintain a constant static pressure (based on output from the capacitive structure of the presented sensor stack). With these advances, the presented research will enable robotic systems to interact with

unstructured environments as well as neuroprosthesis, aiming to restore the natural sense of touch for amputees.

2. Experimental Section

2.1. The Capacitive-Piezoelectric Sensor Stack

Various architectures were used to realize the tactile sensors for electronic skin as shown in Figure S1, Supporting Information.^[2a] The biomimetic tactile-sensing architecture finally used (**Figure 3**) composed of a floating electrode-based capacitive structure in tandem with a piezoelectric structure.^[12a,18] Figure 3a shows the pattern of the three layers of electrodes used for realizing the sensor stack. Figure 3b shows the schematic of various layers of the tactile sensor and Figure 3c shows its equivalent diagram. When static pressure was applied to the sensor, the elastomer (low modulus and high modulus) underwent compression. This resulted in the floating electrode (*F*) coming closer to the signal (*S*) and ground (*G*) electrodes. Further, the effective dielectric constant of the elastomer also changed under compression. As a result, the projected capacitances of the floating electrode onto the interdigitated terminals of the signal and ground electrodes (i.e., C_{FS} and C_{FG}) increased. This resulted in the increase of net capacitance C_{SG} , which was read by a charge time measure unit (CTMU)-based circuit shown in **Figure 4b** and explained in the next subsection. Compared with a parallel plate capacitive structure (Figure S2b, Supporting Information), a coplanar structure with a floating electrode was advantageous as there was no output terminal on the top. In the case of the former, the mechanically weak output terminal may break or get damaged when objects press against the top structure. Compared with a simple coplanar structure with squeezy material (Figure S2c, Supporting Information), the use of the floating gate made the sensor insensitive to the electric property of the objects (refer to Figure S4 in the study by Núñez et al.^[2a]) with which the contact was made. The use of a dual elastomer layer for the capacitive structure was advantageous as during low pressure, the low-modulus elastomer underwent significantly more compression compared with the high-modulus elastomer. At high pressure, the low-modulus elastomer saturated,

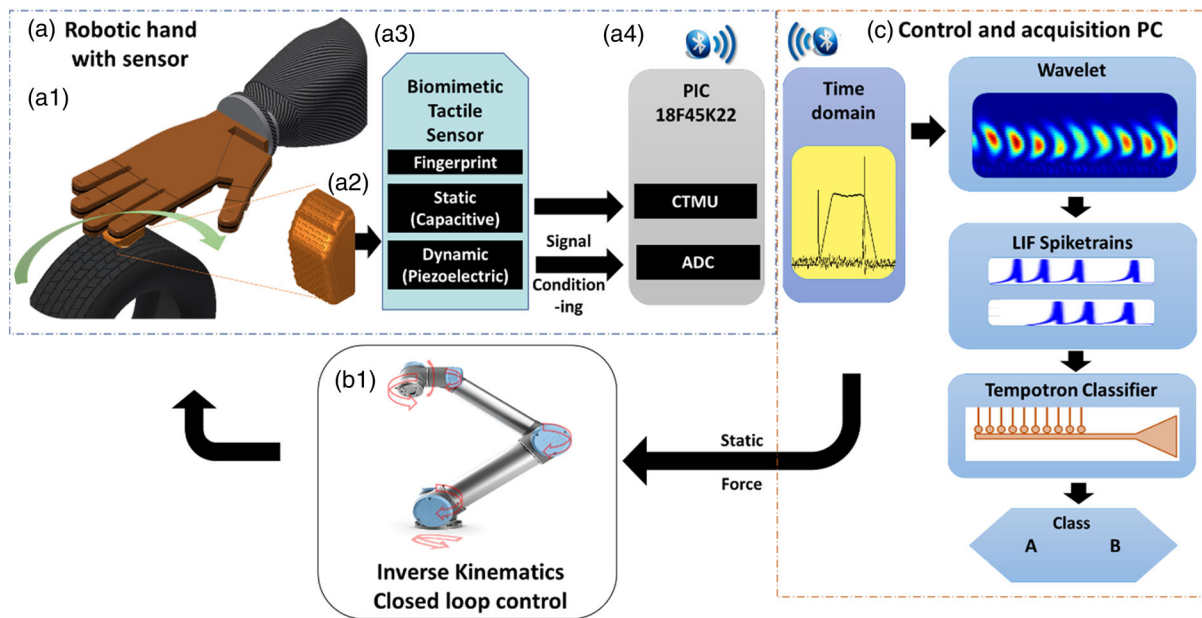


Figure 2. Illustration of the fingerprint-enhanced biomimetic sensor and its application in a tactile pattern recognition system. a1,a2) Capacitive-piezoelectric tandem sensing structure integrated on the distal phalange of the index finger of a 3D-printed hand. a3) The design of the sensing structure comprising fingerprint-like patterns and a capacitive-piezoelectric sensor stack. a4) The PIC 18f45k22 microcontroller-based circuit for readout. The CTMU was used for readout of capacitive signal and the reading of the piezoelectric output involved signal conditioning through an ADC. The data were wirelessly sent to a computer which performs control, data acquisition, and classification. b1) The 6-dof UR5 industrial arm on which the 3D-printed robotic hand was mounted as an end effector. The position and proportional closed-loop control were carried out using the capacitive sensor's output. c) The dynamic sensor's output was converted into Gabor wavelet scalogram and then into spike trains via an LIF model to feed as the input to a tempotron classifier.

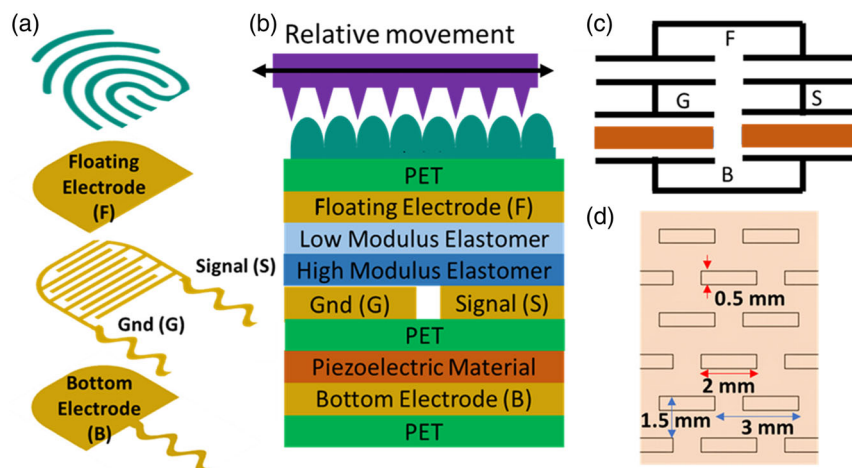


Figure 3. a) Schematic illustration of the biomimetic sensory stack; b) the layers in the sensory stack with fingerprint ridges shown on the top; c) an equivalent diagram of the biomimetic sensory stack; and d) the dimensions of the designed fingerprint ridges realized via 3D printing using ninjaflex.

and the high-modulus elastomer contributed to capacitance change. High-speed dynamic forces acting on the piezoelectric layer caused the piezopotential to be generated between the bottom electrode and ground (V_{BG}) as well as signal electrodes (V_{BS}). Here, V_{BG} was used for further processing. The sensors were fabricated with a facile approach as shown in the study by Navaraj et al.^[12a]

The presented sensor stack was integrated on the distal phalange of the index finger of a 3D-printed prosthetic/robotic hand

as shown in Figure 2a1. The sensor stack was covered with fingerprint ridges structure formed with 3D-printed ninjaflex. The design of the phalange is shown in Figure 2a2. The dimensions of the fingerprints, shown in Figure 3d, included ridges of $500\ \mu\text{m}$ width \times $2\ \text{mm}$ length (dimensions indicated in Figure 3d in red) and of $500\ \mu\text{m}$ thickness (out of plane). The ridges repeated with a vertical pitch of $1500\ \mu\text{m}$ (>3 times higher than typically observed in human fingerprints^[19]) and a

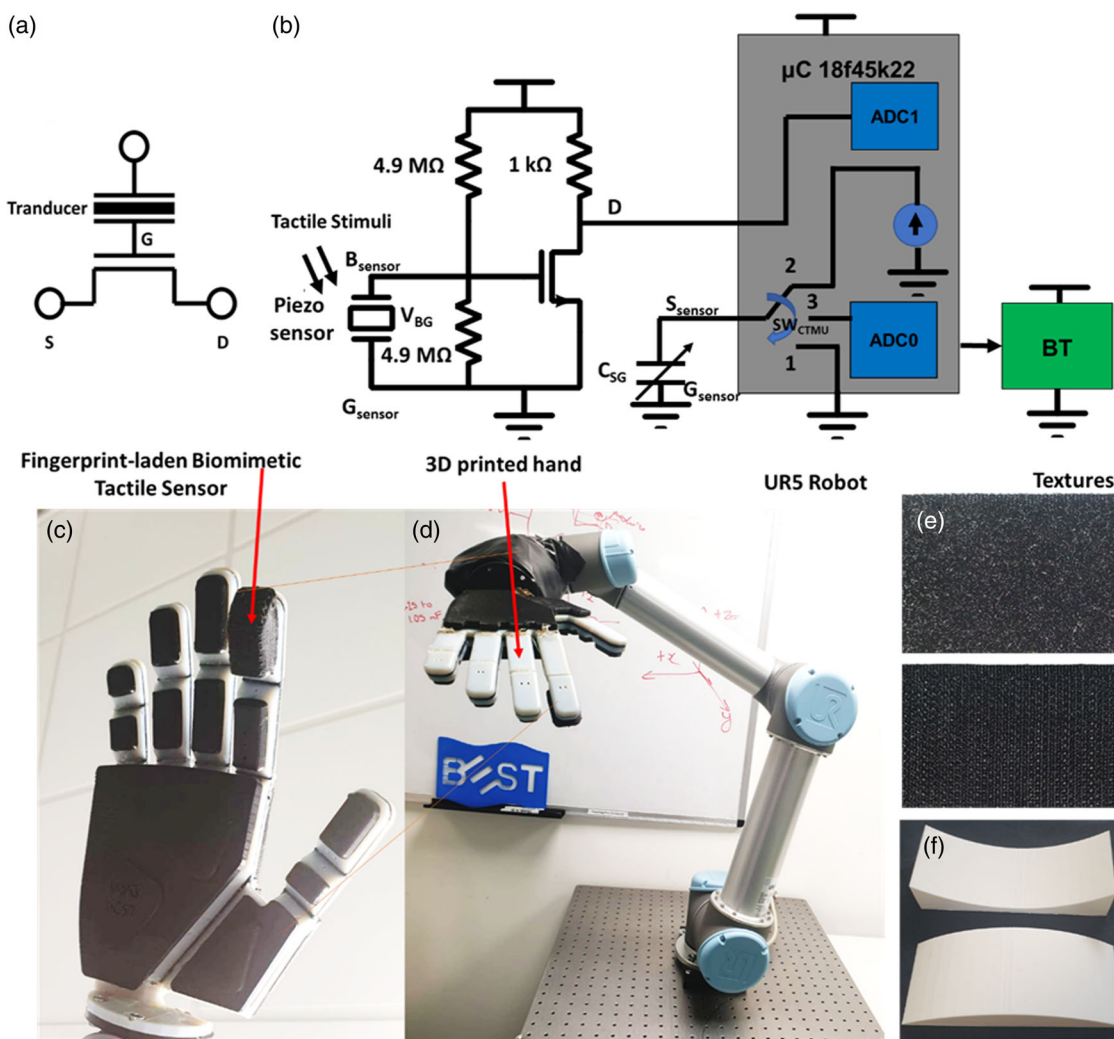


Figure 4. a) Extended gate interface of the piezoelectric sensor to n-channel MOSFET; b) schematic diagram for the static and dynamic sensor readout followed by wireless data transmission; c) 3D-printed hand with a fingerprint-laden biomimetic sensor stack; d) the hand mounted on a UR5 industrial arm; e) various textured surfaces used for classification (above: loop, below: hook); f) and 3D-printed concave (above) and convex (below) structures with a radius of curvature of 10 cm on which the textured surfaces were placed for nonplanar closed-loop scanning.

horizontal pitch of 3000 μm (dimensions indicated in Figure 3d in blue). Alternate ridges were realized in a staggered fashion as shown in Figure 3d. The fingerprint layer on the sensor stack provided robust protection similar to the MRs embedded inside the skin of the human hand. However, there are $>250 \text{ MRs cm}^{-2}$ in the fingertip of the human hand. In our case, we have only one sensory stack comprising two sensor outputs. This work tested whether textures can be perceived with a single biomimetic sensory stack.

The static pressure-sensing performance of the sensory stack was evaluated by applying force of varying amplitudes using a linear stage motor, controlled via LabVIEW program. The linear stage motor's movement was precisely controlled to 1 μm resolution. This was utilized to apply controlled cyclic pulses of force on the sensor of varying amplitudes. The capacitive sensor was tested by measuring the capacitance using Keysight E4980AL Precision LCR Meter, whereas force value was recorded from

a loadcell (Tedea Huntleigh 1004-00.6-JW00-RS). The piezoelectric sensor was characterized by a TIRA vibrator/shaker set up as explained in the study by Dahiya et al.^[20] The sensor was firmly placed on the TIRA shaker/vibrator, which is capable of applying dynamic forces up to 18 N, in a frequency range from 2 Hz to 18 kHz. The shaker was driven by a waveform generator followed by an amplifier (TIRA BAA 120). During experiments, the sensor was sandwiched between a shaker and a uniaxial PCB Piezotronics force sensor, which measured the dynamic force applied by the shaker. The force sensor exhibited a sensitivity of 111 mV N^{-1} , a load range of 44.48 N, and a frequency range from 0.01 Hz to 36 kHz.

2.2. Circuit Interface

The dynamic tactile-sensing element was interfaced with n-metal oxide semiconductor field effect transistor (MOSFET)^[21] in the

extended gate mode,^[15] as shown in Figure 4a, and tested under transient stimuli (P-Press, R-Release). This was for utilizing ultrathin chips with MOSFETs as the backplane circuit elements to realize piezoelectric oxide semiconductor field effect transistors (POSFETs) for tactile sensing.^[21,22] The results are shown in Figure 4c for pulse input and explained in Section 2.3. Figure 4b shows the interface of the piezoelectric element to a common source MOSFET amplifier which helps in converting the dynamic tactile stimuli to voltage output. The voltage was further converted to a digital signal using the inbuilt analog to digital converter (ADC) in a PIC 18f45k22 microcontroller (μC) at a sampling rate of 200 samples s^{-1} . The static capacitive sensors' value was converted into an equivalent digital signal using CTMU, as shown in Figure 4b, similar to the interface for our prior graphene-based sensors.^[2a] Before measurement, the charge in the capacitor to be sensed was discharged completely (SW_{CTMU} in position 1). Then a constant current (I_C) of 55 μA was pumped into the sensor through a switching interface (SW_{CTMU} in position 2) for a fixed time Δt (10 μs). The output voltages (V) of the capacitive sensor were read through the switching interface (SW_{CTMU} in position 3) as a digital value via a 10-bit ADC (ADC0). A change in the output voltage because of the constant current pumped into the capacitive sensors is given by ΔV . As I_C is pumped here for a definite time, by measuring the change in the voltage, the capacitance can be calculated using the equation

$$C = I_C \left(\frac{\Delta V}{\Delta t} \right)^{-1} \quad (1)$$

After digitization, the data from both sensors were sent to a personal computer (PC) via Bluetooth at a baud rate of 115 200 bps. Having a tetherless wireless interface was advantageous for application in prosthetic feedback.^[18]

2.3. Robotic System

The sensor stack was integrated on the distal phalange of the index finger of a robotic/prosthetic hand,^[18] as shown in Figure 4c. The hand was designed and fabricated via 3D printing for application as a myoelectric-controlled prosthesis.^[18] The myoelectric control of the hand is shown in Video S3, Supporting Information. The hand was mounted as an end effector with a custom 3D-printed fixture to a 6-dof UR5 robot (Universal Robotics, Denmark). Both planar and curved textural structures were mounted on a static platform, whereas the UR5 arm was programmed to indent and slide the fingertip over the textures in a closed-loop fashion. An application was implemented based on the robotic operating systems (ROS) package which performed tasks such as acquisition of the data via Bluetooth (based on serial protocol), control of the 6-dof UR5 industrial robotic arm (with the sensor-laden 3D-printed hand as the end effector), closed-loop scanning of textured surfaces, and interface to spiking tempotron classifier (as shown in Figure 2a). Both quasistatic and dynamic sensors were read with a sampling rate of 200 samples s^{-1} . With this arrangement, the sensory stack was tested by applying pressure or tactile stimuli and measuring the normalized relative change for both sensors. The normalization was carried out by measuring the

mean value of each sensory output for 1.5 s which was used as a base value.

2.4. Textures

Naturalistic textures of hook-and-loop fasteners (the hook side and loop side) were used as texture for binary classifications (shown in Figure 4e). The textured surfaces were kept in both planar and mounted conditions on the curved structures of 10 cm radius of curvature as shown in Figure 4f. A total of 200 scans were recorded (comprising 100 planar scans, 50 scans each of concave and convex) and each scan comprised both hook-and-loop textures with a corresponding time tagged via a MATLAB code to indicate the position of the hook and loop with 250 ms overlap with null classification during the offset and onset of the textures. Out of the 200 scans, 160 scans were randomly chosen using a random number generator function in MATLAB and they were used for training, whereas the remaining were used for testing.

2.5. Experimental Protocol

A closed-loop tactile exploration protocol was carried out to obtain the texture signal. Figure S6, Supporting Information, shows the schematic diagram of the proportional control system. The loop-or-hook texture was attached on a planar or curved platform (shown in Figure 4f) which was firmly fixed for the smooth sliding of fingertip over the textured surface by the UR5 arm. The tip of the index finger was initially placed ≈ 5 cm above the textured surface (preparation phase). Then the app waited for the input to continue via the RViz interface of ROS. Following this, the tip was moved in the z-axis until contact was made with the textured surface and a desired contact force was reached (indentation phase). The proportional control loop varied with the depth Z so as to achieve a constant force. While the depth variable was varied proportional to the force through a custom function, the desired depth was achieved by the inbuilt "joint_trajectory_controller" using proportional integral derivative (PID) loops with a repeatability of $\pm 100 \mu\text{m}$. As soon as the indentation completed, the scan phase started with the fingertip sliding over the textured surface for a distance of 6 cm at a speed of $\approx 10 \text{ cm s}^{-1}$. The z-axis was dynamically controlled during this phase to maintain a constant contact force. Upon completion of one forward stride, a reverse stride was also carried out. This was done until a total of nine strides for each texture was reached. Finally, the fingertip was retracted to the initial position (retraction phase). Then the app waited via input prompt through the RViz interface to continue the next scan. Following this, the process was repeated for other textured surfaces.

2.6. Wavelet Transform

Biological research suggests that the temporal frequency channels are linked across audition and touch, and tactile information is processed with a similar approach as that of the audio.^[16] Inspired by this, here, we propose using wavelet-based processing. Cepstral coefficients were widely used for audio processing where usually Fourier transforms were used and later transformed to logarithmic scale.^[23] Instead of carrying out windowed

Fourier transform, we used windowed Gabor wavelet transform (GWT). This was for two reasons: first, wavelets offer localization in time and frequency, thereby capturing temporal variation and second, wavelets are biologically plausible.^[17,24] We have presented results from short-time Fourier transform (STFT) for comparison using the same window size of 100 samples.

2.7. Neuronal Model

Based on the observations from physiological recordings since the 1920s, rate coding was popularly assumed as the information coding mechanism of the neural system^[10a,25] and several artificial systems were modeled and realized based on this. However, rate coding was inadequate, when it came to explaining the strikingly fast response observed in various sensory modalities including somatosensation. For example, rapid response (within ≈ 65 ms) was observed during grasping events.^[26] The information about fingertip events was assumed to be transmitted within a single spike when this fast response

was considered together with the various associated delays such as peripheral nerve conduction, the generation of muscular force, and processing. This indicated that temporal coding was one of the major means through which information was encoded and transmitted in the biological tactile-sensing system. Considering this, the normalized wavelet amplitudes from different wavelet bins were encoded into latency-coded spike trains. An LIF model was used for spike modeling as it is computationally efficient. The normalized post-synaptic potential (PSP) in this case is given by

$$PSP_{\text{Norm}}(t) = K(t - t_i) = V_0 \left(\exp\left(\frac{-(t-t_i)}{\tau}\right) - \exp\left(\frac{-(t-t_i)}{\tau_s}\right) \right) \quad (2)$$

where t_i , τ , and τ_s are the i th spike time, decay time constants of membrane integration, and synaptic currents, respectively.^[27] V_0 is the normalization factor. The spike window per bin was kept as 100 samples. The amplitude of the spike determined the position of the spike within this window as shown

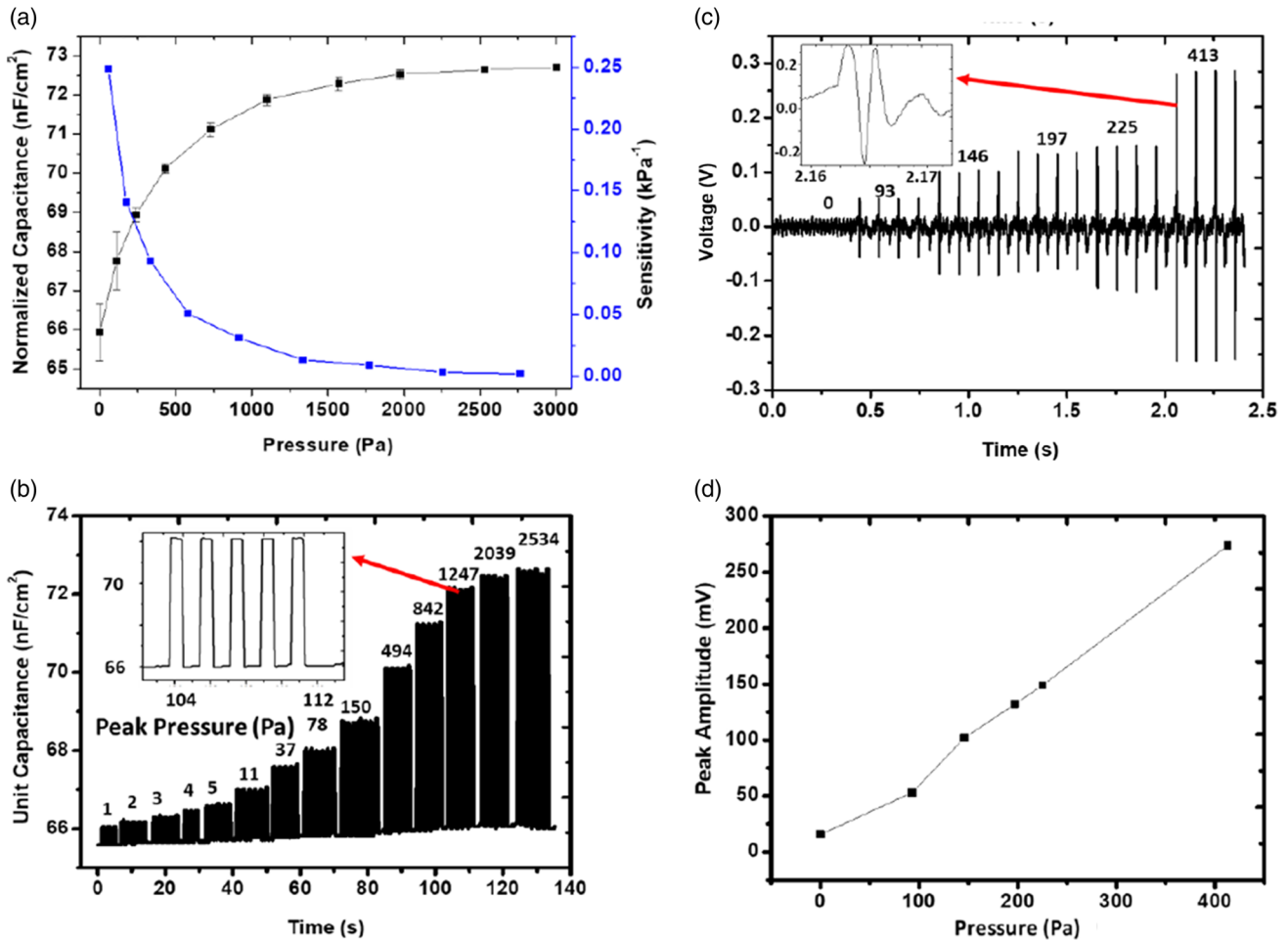


Figure 5. a) Quasistatic characteristics of the capacitive sensor element showing signal-ground capacitance (C_{SG}) versus pressure; b) transient characteristics showing capacitance C_{SG} of the capacitive sensor element under cyclic pressure test (inset: zoomed-out view of the response at a peak cycle pressure of ≈ 1.25 kPa); c) voltage between the bottom and ground electrode (V_{BG}) measured across the piezoelectric sensor element under cyclic pressure (inset: zoomed-out view of response at a peak cycle pressure of ≈ 413 Pa); and d) peak pressure versus peak amplitude V_{BG-Pk} of the piezoelectric sensor. Reproduced with permission.^[12a] Copyright 2018, IEEE.

in Figure S4, Supporting Information. Stronger the amplitude, faster the spike was elicited within the time span.

2.8. Tempotron Classifier

The spike trains were classified using a tempotron classifier.^[27] The biologically plausible STDP algorithm was used to train the tempotron classifier. The spike trains based on the LIF model from various wavelet bins as explained earlier were given as inputs to the neuron. The subthreshold membrane voltage of the tempotron was the weighted sum of the PSPs from all incoming spikes from different wavelet bins^[27]

$$V(t) = \sum_i \omega_i \sum_{t_i} K(t - t_i) + V_{\text{rest}} \quad (3)$$

The weights of the input synapses were adjusted to emit a spike output for the matching target category using a supervised learning strategy. Here, two tempotrons were used, one for detecting “hook” and the other for “loop.” For each, the synaptic efficacy was adjusted when no output spike was elicited for the target category to the value given by

$$\Delta \omega_i = \lambda \sum_{t_i < t_{\text{max}}} K(t_{\text{max}} - t_i) \quad (4)$$

where a learning rate (λ) of 0.005 was used. t_{max} denotes the time at which the PSP reached the maximum value.

3. Results and Discussion

Figure 5 shows the output characteristics of the two types of tactile sensing structures in the sensory stack. The static capacitive sensor’s characteristic C_{SC} shown in Figure 3a was found to be nonlinear with very high sensitivity (up to 0.25 kPa^{-1}) in the lower-pressure ($<100 \text{ Pa}$) range whereas it showed lower sensitivity in higher pressure (0.002 kPa^{-1} at $\approx 2.5 \text{ kPa}$). It should be noted that the tactile MRs in the human hand also exhibit a nonlinear response with a similar sensitivity variation qualitatively.^[28] This can be compared with the typical sensitivity of human tactile sensing which can sense the pressure involved in breathing and feather touch (from 1 Pa to 1 kPa) to everyday object manipulation ($1\text{--}100 \text{ kPa}$).^[29] The quasistatic characteristics of this sensor were measured only for low-pressure regimes

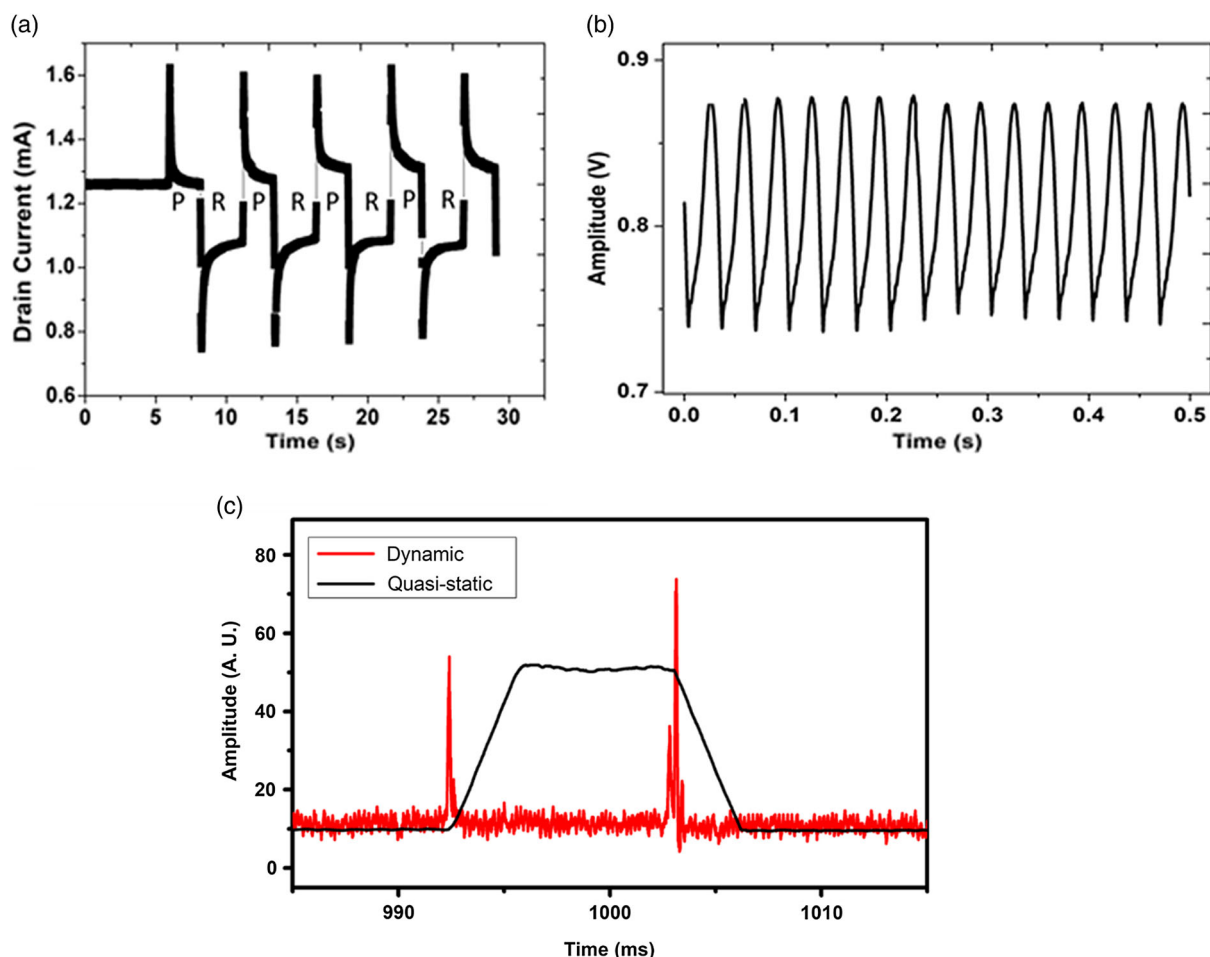


Figure 6. a) Transient response of drain current with the dynamic tactile sensor in the extended gate POSFET mode; b) output of the dynamic tactile sensor circuit (interfaced in an extended gate mode to a common source n-MOSFET amplifier); and c) plot of the wirelessly transmitted live data acquired via the rqtplot of the ROS package (Video S5, Supporting Information).

as the resulting application on the 3D-printed hand (a maximum load of 3 kg) cannot withstand higher pressures in the order of 100 kPa. The transient characteristics of the same capacitive structure are shown in Figure 5b. Assuming that the fringe capacitance between the interdigitated electrodes of capacitance C_{SG} is negligible, C_{SG} is related to C_{SF} and C_{FG} as

$$\frac{1}{C_{SG}} = \frac{1}{C_{SF}} + \frac{1}{C_{FG}} \quad (5)$$

Normalized unit areal capacitance with symmetry ($C_{Norm-SF} = C_{Norm-FG}$) is related to normalized low-modulus ($C_{Norm-LME}$) and high-modulus ($C_{Norm-HME}$) unit areal capacitances as

$$\frac{1}{C_{Norm-SG}(P)} = \frac{2}{C_{Norm-FG}(P)} = 2 \left(\frac{1}{C_{Norm-LME}(P)} + \frac{1}{C_{Norm-HME}(P)} \right) \quad (6)$$

$$C_{Norm-XME}(P) = \frac{\epsilon_0 \epsilon_{XME}(P)}{2 \left(d_{0-XME} - \frac{P d_{0-XME}}{Y_{XME}} \right)} \quad (7)$$

where ϵ_0 is the permittivity of free space, $\epsilon_{XME}(P)$ is the effective relative dielectric constant of the low- or high-modulus elastomeric stack under pressure, and d_{0-XME} and Y_{XME} are the initial thickness and Young's modulus of the particular elastomeric stack, respectively. The aforementioned equations imply an increase in capacitance under pressure as observed in Figure 5b.

The voltage output V_{BG} of the piezoelectric stack at 10 Hz input of various peak pressure amplitudes (in Pa) is shown in Figure 5c. Figure 5d shows peak voltage versus peak pressure amplitude of the sensor. The force applied to piezoelectric transducer results in a net dipole moment within the piezoelectric material due to the noncentrosymmetric property of the material, resulting in the generation of piezopotential. The relationship between applied force and charge generated can be approximately described as^[14a]

$$Q = d_{33} F \quad (8)$$

where d_{33} is the piezoelectric coefficient and F is the applied force. As the generated charge density is linearly dependent on the applied pressure (force per unit area), the generated piezopotential is directly dependent on the magnitude of pressure. Thus, a higher magnitude of force/pressure results in a higher magnitude of piezopotential. The piezoelectric sensor structure exhibited a sensitivity of 2.28 kPa^{-1} . Figure S6, Supporting Information shows the hysteretic characteristics of the sensors under a pressure loading–unloading test. The capacitive sensory structure exhibited hysteresis resulting in $<7.3\%$ variation for the applied pressure range which could be attributed mainly to the viscoelastic creep in the elastomeric layer.^[30] The piezoelectric sensory structure didn't exhibit any observable hysteretic variation. The results of the extended gate POSFET are shown in Figure 6a for pulse input (P-Press, R-Release). In this configuration, the pressure stimulus is converted into variation in the drain current. The response of the extended gate POSFET amplifier for a sinusoidal pressure stimulus via TIRA shaker for

$\approx 23 \text{ Pa}$ peak pressure stimulus of 30 Hz continuous input is shown in Figure 6b. The common source MOSFET amplifier helps in converting dynamic tactile stimuli to voltage output. There is a slight nonlinearity observed in the negative cycle. Neural networks are known to be inherently robust against such nonlinearity in the system. The sensory stack along with the interface circuit and Bluetooth readout was tested for real-time measurement of both static and dynamic sensors by applying pressure on the phalange. The net output from both quasistatic and dynamic sensors received wirelessly from the readout circuit in the robotic hand was monitored via the rqtplot tool of the ROS package, a snapshot of which is shown in Figure 6c, and the corresponding video is shown in Video S5, Supporting Information. As observed, both static and dynamic data were read effectively by the developed wireless readout interface. It can be observed the dynamic sensor responds instantaneously at the onset or offset of applied pressure with the ability to capture the millisecond range transition whereas the static sensor reaches its stable state after 300 ms. The dynamic sensor structure's output was rectified

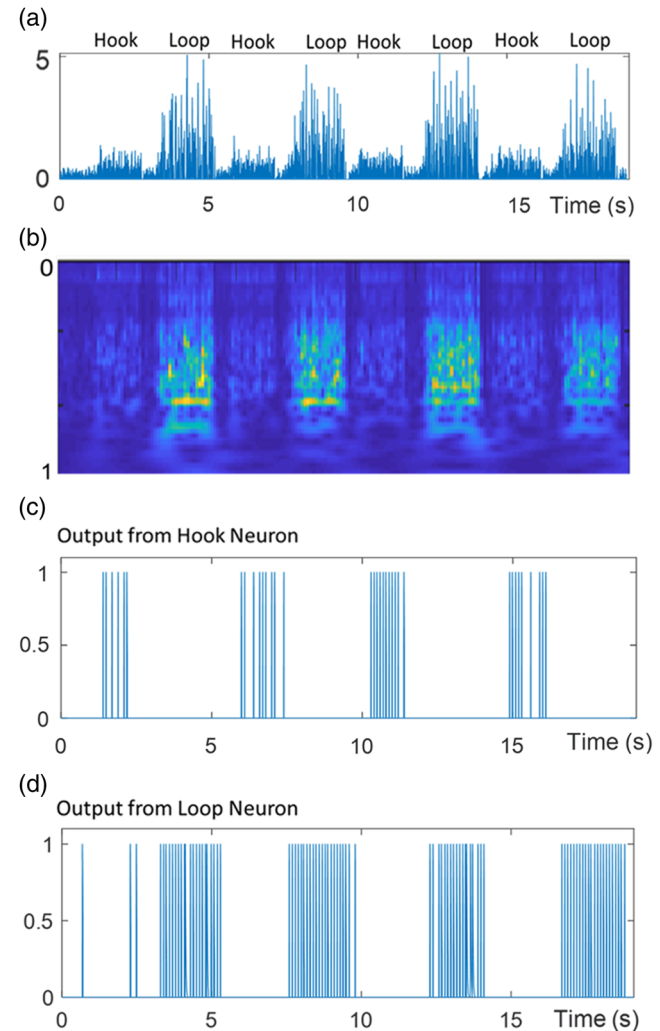


Figure 7. a) A typical recorded signal from the dynamic scan; b) Gabor wavelet scalogram; and c,d) output from the tempotron classifier neuron corresponding to c) hook and d) loop.

programmatically after baseline correction because of which the change is mainly observed in the positive direction.

Figure 7a shows a typical recorded signal where the corresponding naturalistic texture is tagged earlier. The transition gap is also visible between them. The loop was found to give a higher amplitude compared with the hook, mainly owing to the loop getting hooked to the fingerprint patterns and then getting released, which is reflected as a strong amplitude variation. Figure 7b shows the typical normalized scalogram, which was used as a feature set to generate spike trains. Figure 8 shows training error versus number of epochs during the training of the neural network with two different features (STFT and

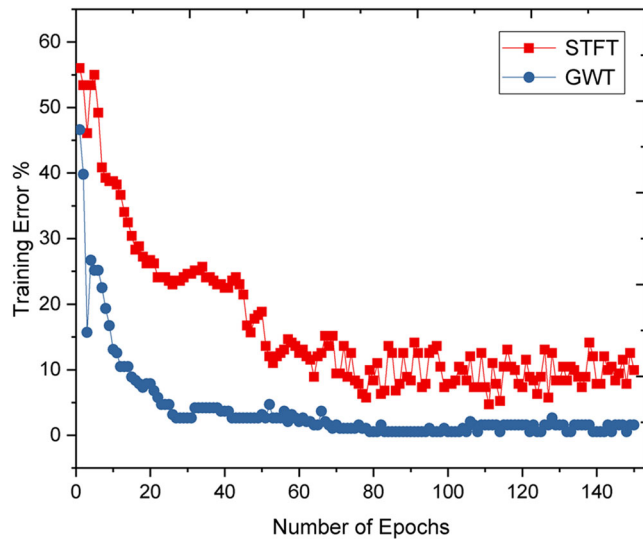


Figure 8. Training error versus number of epochs comparing STFT and GWT-based features.

GWT) used to generate spike trains. The STFT-based approach provides a maximum classification accuracy of 95.3%, whereas the GWT-based approach offers 99.45% for the same windowed time. Figure 7c,d shows the output response from the two classification neurons corresponding to the hook and loop, respectively. The output spike response can be observed to be accurate for the test pattern.

Table 1 compares the works related to texture classification carried out with tactile sensors using spike coding. Compared with the previous research, we have aimed to achieve structural mimicry (mimicking sensing structure in terms of SA, FA, and fingerprints) and neuromimicry (mimicking neural data processing, i.e., spike trains from wavelets followed by the tempotron classifier system) concepts by leveraging on observations in biological tactile sensing. Additionally, this work also involved scanning textures on planar and nonplanar curved surfaces. Prior works have reported texture scanning on planar surfaces only. As explained earlier, the scanning of planar and nonplanar curved surfaces was achieved by the proportional closed-loop control of the index finger position of the 3D-printed hand attached to a 6-dof UR5 robot. Figure S7b, Supporting Information, shows a typical trajectory of the end effector showing the position (X, Y, and Z) and orientation (yaw, pitch, and roll) during the concave nonplanar scans of 10 cm radius of curvature. Various stages of the scanning process can be observed during the preparation phase when the end effector goes to the desired X and Y position and orientation. This is followed by the approach phase, during which Z decreases until contact is made. The forward and reverse scans (a total of nine scans in the Y direction) on the curved structure are carried out. Z adapts during this scan as per the surface. This feedback control along with the flexibility of thermoplastic polyurethane (TPU)-based joints of the 3D-printed prosthetic hand helps in achieving a compliant scan over the nonplanar surface. The end effector is retracted after the scan. While the implemented system is able to perform

Table 1. Comparison of tactile-based texture recognition with spike coding.

| Sensor structure | Features | Decoding | Implementation | Textures | Accuracy | Year and Ref. |
|--|---|--|---|---|------------------------------------|----------------------|
| MEMS-based piezoresistive 2×2 sensors | Amplitude to rate-coded spike trains (Izhikevich) | Both ISI-CV kNN and precise spike timing (VPd) | Mechatronic sliding platform | Ten naturalistic textures | Maximum 97% | 2015 ^[31] |
| Three piezoceramic off-the-shelf acceleration sensors | Nonlinear features of spike trains (LIF) in the frequency domain | Recurrent SNN | 6-dof robotic arm. Open-loop scanning | 18 metal surface textures | Overall 65.6% | 2016 ^[32] |
| Piezoelectric (PVDF) | Amplitude to spike trains (Izhikevich) | kNN | Manual sliding over textures | Eight rough surfaces | Maximum 77.6 % | 2017 ^[33] |
| Three piezoresistive taxels | Quasistatic piezoresistive output converted into three spike trains/sensors for FA and SA | ELM classifier | Kuka robotic arm. Force control for contact. Open-loop scanning | Ten textures | Maximum 92% | 2018 ^[34] |
| Fingerprint-enhanced capacitive-piezoelectric tandem sensors | Frequency to temporal spike trains | Tempotron classifier | Sensor stack integrated on 3D-printed robotic hand mounted on a UR5 robot arm. Closed-loop scanning on four uneven surfaces | Two naturalistic textures but wrapped on various surfaces | 99.5 % with GWT vs 95.3% with STFT | This work |

ISI-CV—Coefficient of the variance (CV) of interspike interval (ISI); kNN—k-Nearest neighbors algorithm; VPd—Victor Purpura distance; LIF—leaky integrate-and-fire; dof—degree-of-freedom; ELM—Extreme learning machine; STFT—Short time Fourier transform; GWT—Gabor wavelet transform.

binary classification reliably, the classification of more textures needs to be carried out to test the efficiency and the potential of the presented system.

Received: June 16, 2019
Revised: August 12, 2019
Published online: September 20, 2019

4. Conclusion

The sensitive capacitive-piezoelectric flexible sensing skin with fingerprint-like patterns presented here is able to detect and discriminate between spatiotemporal tactile stimuli such as static and dynamic pressures and textures. The dynamic tactile sensor exhibited a sensitivity of 2.28 kPa^{-1} whereas the static sensor exhibited nonlinear characteristics varying from high sensitivity of 0.25 kPa^{-1} in the low-pressure range ($<100 \text{ Pa}$) to 0.002 kPa^{-1} in high pressure ($\approx 2.5 \text{ kPa}$). The extended-gate POSFET configuration of the dynamic sensor is shown here as a step toward bendable ultrathin high-density tactile sensing chips integrated in the 3D-printed hand to provide distributed sensing and computing at par or exceeding human tactile sensing. The output from the presented sensor under a closed-loop tactile scan, carried out with an industrial robotic arm, was given as latency-coded spike trains to a spiking neural network (SNN) tempotron classifier system. Using the system, we demonstrated binary naturalistic texture classification with a maximum accuracy of 99.45%. It also demonstrates that a single sensory stack may be sufficient for texture classification although further study on a greater number of textures has to be carried out to find its limit. Further, considering the number of wavelet bins, such processing may be possible in a cortical level. Biomimicry of the peripheral to cortical transport also has to be incorporated in the model to consider a realistic case. The work could be advanced in several directions such as realization of the sensory stack for all phalanges, fingers, and hands, for advanced grasping and tactile exploration, using not just temporal data but spatiotemporal data for SNN, incorporating sensemaking layers. The presented bioinspired skin will aid the development of advanced robotic systems to be able to interact with unstructured environments as well as neuroprosthesis, aiming to restore the natural sense of touch for amputees.

Supporting Information

Supporting Information is available from the Wiley Online Library or from the author.

Acknowledgements

This work was supported by EPSRC through Engineering Fellowship for Growth (EP/M002527/1 and EP/R029644/1).

Conflict of Interest

The authors declare no conflict of interest.

Keywords

capacitive-piezoelectric sensors, eSkins, spiking neural networks, tactile sensors, tempotron classifier

- [1] a) R. Dahiya, *Proc. IEEE*, **2019**, *107*, 247; b) L. E. Osborn, A. Dragomir, J. L. Betthausen, C. L. Hunt, H. H. Nguyen, R. R. Kaliki, N. V. Thakor, *Sci. Robot.* **2018**, *3*, eaat3818.
- [2] a) C. G. Núñez, W. T. Navaraj, E. O. Polat, R. Dahiya, *Adv. Funct. Mater.* **2017**, *27*, 1606287; b) K. Takei, W. Gao, C. Wang, A. Javey, *Proc. IEEE*, **2019**, <https://doi.org/10.1109/JPROC.2019.2907317>; c) S. Bauer, S. Bauer-Gogonea, I. Graz, M. Kaltenbrunner, C. Keplinger, R. Schwödiauer, *Adv. Mater.* **2014**, *26*, 149; d) N. Yogeswaran, W. Dang, W. T. Navaraj, D. Shakhthivel, S. Khan, E. O. Polat, S. Gupta, H. Heidari, M. Kaboli, L. Lorenzelli, C. Gordon, R. Dahiya, *Adv. Robot.* **2015**, *29*, 1359; e) R. Dahiya, W. T. Navaraj, S. Khan, E. Polat, *Inf. Disp.* **2015**, *31*, 5; f) L. Manjakkal, W. T. Navaraj, C. G. Núñez, R. Dahiya, *Adv. Sci.* **2019**, *6*, 1802251.
- [3] a) W. W. Lee, S. L. Kukreja, N. V. Thakor, *Front. Neurosci.* **2017**, *11*, 5; b) J. Park, M. Kim, Y. Lee, H. S. Lee, H. Ko, *Sci. Adv.* **2015**, *1*, e1500661; c) S. Hannah, A. Davidson, I. Glesk, D. Uttamchandani, R. Dahiya, H. Gleskova, *Org. Electron.* **2018**, *56*, 170.
- [4] a) S. Luo, J. Bimbo, R. Dahiya, H. Liu, *Mechatronics* **2017**, *48*, 54; b) W. T. Navaraj, C. Garcia, D. Shakhthivel, V. Vinciguerra, F. Labeau, D. Gregory, R. Dahiya, *Front. Neurosci.* **2017**, *11*, 501; c) S. Decherchi, P. Gastaldo, R. Dahiya, M. Valle, R. Zunino, *IEEE Trans. Robot.* **2011**, *34*, 1.
- [5] a) B. C.-K. Tee, A. Chortos, A. Berndt, A. K. Nguyen, A. Tom, A. McGuire, Z. C. Lin, K. Tien, W.-G. Bae, H. Wang, *Science* **2015**, *350*, 313; b) Y. Kim, A. Chortos, W. Xu, Y. Liu, J. Y. Oh, D. Son, J. Kang, A. M. Foudeh, C. Zhu, Y. Lee, *Science* **2018**, *360*, 998; c) C. J. Wan, L. Q. Zhu, Y. H. Liu, P. Feng, Z. P. Liu, H. L. Cao, P. Xiao, Y. Shi, Q. Wan, *Adv. Mater.* **2016**, *28*, 3557.
- [6] F. Liu, W. Taube, N. Yogeswaran, D. Gregory, R. Dahiya, Transforming the Short-term Sensing Stimuli to Long-term e-skin Memory, presented at 2017 IEEE Sensors, Glasgow **2017**.
- [7] a) R. Dahiya, G. Metta, M. Valle, G. Sandini, *IEEE Trans. Robot.* **2010**, *26*, 1; b) R. Dahiya, M. Valle, *Robotic Tactile Sensing – Technologies and System*, Springer, Dordrecht **2013**.
- [8] R. S. Johansson, J. R. Flanagan, *Tactile Sensory Control of Object Manipulation in Humans*, Academic Press, New York, NY **2008**.
- [9] E. B. Goldstein, J. Brockmole, *Sensation and Perception*, Cengage Learning, Boston, MA, **2016**.
- [10] a) R. S. Johansson, J. R. Flanagan, *Nat. Rev. Neurosci.* **2009**, *10*, 345; b) J. H. Kaas, *The Senses: A Comprehensive Reference. 6. Somatosensation*, Elsevier, Amsterdam **2008**.
- [11] M. Hollins, S. R. Risner, *Percept. Psychophys.* **2000**, *62*, 695.
- [12] a) W. T. Navaraj, O. Ozioko, R. Dahiya, in IEEE Sensors, New Delhi, India 2018; b) R. Dahiya, P. Mittendorfer, M. Valle, G. Cheng, V. Lumelsky, *IEEE Sens. J.* **2013**, *13*, 4121.
- [13] a) J. Scheibert, S. Leurent, A. Prevost, G. Debrégeas, *Science* **2009**, *323*, 1503; b) R. S. Dahiya, M. Gori, *J. Neurophysiol.* **2010**, *104*, 1.
- [14] a) N. Yogeswaran, W. T. Navaraj, S. Gupta, F. Liu, V. Vinciguerra, L. Lorenzelli, R. Dahiya, *Appl. Phys. Lett.* **2018**, *113*, 014102; b) A. Polishchuk, W. Navaraj, H. Heidari, R. Dahiya, *Procedia Engineering* **2016**, *168*, 1605.
- [15] C. García Núñez, F. Liu, W. T. Navaraj, A. Christou, D. Shakhthivel, R. Dahiya, *Microsyst. Nanoeng.* **2018**, *4*, 22.
- [16] J. M. Yau, J. B. Olenczak, J. F. Dammann, S. J. Bensmaia, *Curr. Biol.* **2009**, *19*, 561.
- [17] C. F. Stevens, *Proc. Natl. Acad. Sci.* **2004**, *101*, 15524.

- [18] W. T. Navaraj, O. Ozioko, H. Nassar, R. Dahiya, Prosthetic Hand with Biomimetic Tactile Sensing and Force Feedback, presented at IEEE International Symposium on Circuits and Systems, Sapporo, Japan, 2019.
- [19] M. A. Acree, *Forensic Sci. Int.* **1999**, *102*, 35.
- [20] R. Dahiya, D. Cattin, A. Adami, C. Collini, L. Barboni, M. Valle, L. Lorenzelli, R. Oboe, G. Metta, F. Brunetti, *IEEE Sens. J.* **2011**, *11*, 3216.
- [21] W. T. Navaraj, S. Gupta, L. Lorenzelli, R. Dahiya, *Adv. Electron. Mater.* **2018**, *4*, 1700277.
- [22] a) S. Gupta, W. T. Navaraj, L. Lorenzelli, R. Dahiya, *NPJ Flex. Electron.* **2018**, *2*, 1; b) S. Caviglia, L. Pinna, M. Valle, C. Bartolozzi, *IEEE Trans. Circuits Syst. Regul. Pap.* **2016**, *64*, 1421.
- [23] N. Mogran, H. Bourlard, H. Hermansky, *Speech Processing in the Auditory System*, Springer, New York **2004**, pp. 309–338.
- [24] T. Chi, P. Ru, S. A. Shamma, *J. Acoust. Soc. Am.* **2005**, *118*, 887.
- [25] E. D. Adrian, *J. Physiol.* **1926**, *61*, 49.
- [26] R. S. Johansson, I. Birznieks, *Nat. Neurosci.* **2004**, *7*, 170.
- [27] R. Gutig, H. Sompolinsky, *Nat. Neurosci.* **2006**, *9*, 420.
- [28] L. Skedung, M. Arvidsson, J. Y. Chung, C. M. Stafford, B. Berglund, M. W. Rutland, *Sci. Rep.* **2013**, *3*, 2617.
- [29] a) M. L. Hammock, A. Chortos, B. C. Tee, J. B. Tok, Z. Bao, *Adv. Mater.* **2013**, *25*, 5997; b) C. G. Nunez, L. Manjakkal, R. Dahiya, *NPJ Flex. Electron.* **2019**, *3*, 1; c) Y. Lee, J. Park, S. Cho, Y.-E. Shin, H. Lee, J. Kim, J. Myoung, S. Cho, S. Kang, C. Baig, *ACS Nano* **2018**, *12*, 4045; d) C. Dagdeviren, Y. Su, P. Joe, R. Yona, Y. Liu, Y.-S. Kim, Y. Huang, A. R. Damadoran, J. Xia, L. W. Martin, *Nat. Commun.* **2014**, *5*, 4496.
- [30] S. C. B. Mannsfeld, B. C. K. Tee, R. M. Stoltenberg, C. V. H. H. Chen, S. Barman, B. V. O. Muir, A. N. Sokolov, C. Reese, Z. N. Bao, *Nat. Mater.* **2010**, *9*, 859.
- [31] U. B. Rongala, A. Mazzoni, C. M. Oddo, *IEEE Trans. Neural Netw. Learn. Syst.* **2015**, *28*, 819.
- [32] K. E. Friedl, A. R. Voelker, A. Peer, C. Elias Smith, *IEEE Robot. Autom. Lett.* **2016**, *1*, 516.
- [33] Y. Zhengkun, Z. Yilei, *Neurocomputing* **2017**, *244*, 102.
- [34] M. Rasouli, Y. Chen, A. Basu, S. L. Kukreja, N. V. Thakor, *IEEE Trans. Biomed. Circuits Syst.* **2018**, *12*, 313.